Nano Energy 90 (2021) 106609

Contents lists available at ScienceDirect

Nano Energy

journal homepage: www.elsevier.com/locate/nanoen

Metallic nanoparticle-on-mirror: Multiple-band light harvesting and efficient photocurrent generation under visible light irradiation

Alexander B. Tesler [a,*], Takumi Sannomiya [b], Seyedsina Hejazi [a], Reza Mohammadi [c], Nicolas Vogel [c], Marco Altomare [d], Patrik Schmuki [a,e,f,**]

[a] Department of Materials Science and Engineering, Institute for Surface Science and Corrosion WW4-LKO, University of Erlangen-Nuremberg, Martensstrasse 7, D-91058 Erlangen, Germany
[b] Department of Materials Science and Engineering, School of Materials and Chemical Technology, Tokyo Institute of Technology, 226-8503 Yokohama, Kanagawa, Japan
[c] Department of Chemical and Biological Engineering, Institute of Particle Technology, University of Erlangen-Nuremberg, Cauerstrasse 4, D-91058 Erlangen, Germany
[d] Photocatalytic Synthesis Group (PCS), Faculty of Science and Technology, MESA+ Institute for Nanotechnology, University of Twente, P.O. Box 217, 7500 AE Enschede, The Netherlands
[e] Chemistry Department, Faculty of Sciences, King Abdul-Aziz University, 80203 Jeddah, Saudi Arabia
[f] Regional Centre of Advanced Technologies and Materials, Palacky University, Listopadu 50 A, 772 07 Olomouc, Czech Republic

ARTICLE INFO

Keywords:
Titanium dioxide
Metallic nanoparticles
Fabry-Pérot interference
Photoelectrochemistry
Water splitting
Interband excitations

ABSTRACT

We present a photoanode concept for photoelectrochemical (PEC) water splitting based on metal nanoparticles (Au, Ag, Cu) deposited on a Ti mirror (NPoM) to photosensitize an intermediate TiO_2 layer to induce the harvesting of light with sub-bandgap photon energies. The generation of hot electron-hole pairs in metallic nanostructures can occur either by intraband excitation, *i.e.*, plasmon electrons, or by the interband transition of the d-band electrons to the unoccupied conduction band states. Our results demonstrate that the underlying Ti mirror significantly amplifies the PEC activity of such NPoM systems in the visible spectral range. We show that the PEC enhancement in the visible spectral range is not limited to the intraband excitations but is affected mainly by the light trapping pathway within the TiO_2 layer, *i.e.* due to a favorable interplay between thin-film interference cavity modes with both intraband and interband excitations. Among tested metals, Cu and Ag NPs demonstrate a ~3-fold higher enhancement factor than that of Au NPs, while in both former cases the nature of the excited electrons is different. The experimentally determined internal quantum efficiency demonstrates alternating behavior with wavelength showing higher efficiencies at short wavelengths, which is attributed to the reduced Schottky barrier of the NPoMs at constructive interference maxima.

1. Introduction

Harnessing the solar energy for photoelectrochemical (PEC) water splitting through catalysis is considered a promising route for clean energy generation to cope up with the current energy crisis. Since the pioneering work of Fujishima and Honda in 1972 [1], PEC systems have been widely studied as green energy alternatives to conventional fuel technology [2,3]. Among available applications, artificial photosynthesis [4], PEC water splitting to generate H_2 gas [2,3,5], and solar cells [6,7] are of particular importance. However, despite an intensive study during the last 50 years, it is still challenging to develop processes to obtain efficient renewable sources and, in particular, enhanced photoactivity in the visible spectral range [8,9].

According to the fundamental mechanism of photo(electro)catalysis, it is notable that light absorption for the generation of energetic charge carriers is the governing factor of the process [10]. To improve photo-activity, enhancing solar light absorption of the photocatalytic systems is essential. However, the traditional semiconducting materials used in the photocatalytic applications have a wide bandgap meaning that they absorb light in the UV region, which is only 3–5% of the solar spectrum [11,12], while the other, *i.e.*, ~46% of visible and ~49% of NIR light are only barely utilized. Extending the light absorption range

* Corresponding author.
** Corresponding author at: Department of Materials Science and Engineering, Institute for Surface Science and Corrosion WW4-LKO, University of Erlangen-Nuremberg, Martensstrasse 7, D-91058 Erlangen, Germany.
E-mail addresses: alexander.tesler@fau.de (A.B. Tesler), schmuki@ww.uni-erlangen.de (P. Schmuki).

https://doi.org/10.1016/j.nanoen.2021.106609
Received 19 July 2021; Received in revised form 13 September 2021; Accepted 3 October 2021
Available online 8 October 2021

of the photoelectrochemical materials to visible-NIR regions is a practical solution for more efficient utilization of solar energy to improve the overall solar conversion efficiency [13]. However, it is difficult to harvest the long-wavelength light efficiently for solar-to-chemical energy conversion due to its low photonic energy. Such low energy nature is unable to excite the typical large bandgap semiconductors being incompetent to photo-induce charge carriers separation [14].

Among available semiconducting materials, titanium dioxide (TiO_2) is one of the promising materials for photocatalytic applications due to its outstanding physicochemical properties such as chemical stability [15], relatively low cost, as well as large availability [16]. Furthermore, the position of TiO_2 valence (VB) and conduction (CB) bands fits well with the splitting of water into O_2 and H_2 gases [17,18]. However, the wide bandgap of TiO_2, which is 3.0 – 3.2 eV depending on the crystallographic phase (anatase or rutile), restricts its efficiency setting a limit to light absorption to UV photons [16,19]. Numerous approaches such as bandgap engineering *via* doping by non-metal elements (N, C, H, P, B) [9,20], metals (Fe, Cu, Cr, V) [21], as well as sensitization of TiO_2 surface with dye molecules or quantum dots [22,23], among others, have been applied to shift the bandgap of the TiO_2 to the visible spectral range.

Another feasible alternative is to modify the surface of TiO_2 with metallic nanostructures that enable localized surface plasmon resonance (LSPR) phenomena [24]. The interaction of light with nanostructured metals results in the excitation of collective charge-density oscillations and the appearance of a strong LSPR extinction band(s) in the vis/NIR range [25]. It is well known that the absorption of light by LSPR of metal nanostructures is tunable and depends strongly on the size, shape, aspect ratio of the nanostructures, the dielectric properties of both metal, and the surrounding environment [25,26].

When deposited on a semiconductor support, plasmonic nanostructures can generate charge carriers, so-called "hot" electrons, which can be injected into the semiconductor substrate [27]. Upon visible light illumination, hot electrons/holes are generated in Au nanoparticles (NPs), *e.g.* deposited on TiO_2 such "hot" carriers can be utilized in a PEC configuration for water splitting. Several plasmon-induced Au-TiO_2 photoelectrode configurations have been proposed to enhance the PEC activity, varying the TiO_2 layer geometry from planar dense to mesoporous films, or arrays of one-dimensional nanostructures such as nanotubes, nanowires, or nanorods [16]. At the same time, plasmonic Au nanoparticles (NPs) can be synthesized either by wet chemical synthesis from Au precursors using reducing chemical agents or photo-deposition [28,29], or by physical vapor deposition techniques such as resistive or e-beam evaporation [30,31], and magnetron or Ar-plasma sputtering [32].

An alternative way to increase the PEC efficiency is to place the plasmonic NPs on a thin transparent semiconducting layer supported by a metallic mirror substrate (Nano Particles-on-Mirror, NPoM) [33]. The NPoM configuration exhibits multiple resonance peaks due to hybridization between localized surface plasmons in the nanoparticles and Fabry−Perót cavity mode reflections within the transparent semiconducting spacer caused by the highly reflective mirror substrate [34]. The NPoM configuration has shown promising characteristics for surface-enhanced spectroscopies used for bio- and chemical sensing [35–37]. In all these cases, however, the spacer is a dielectric material pre-deposited or formed *in situ* by oxidation of the metallic mirror [31,35,37]. While reports on plasmon-enhanced photocurrent in TiO_2–noble metal NP structures date back to 1996 [38], the NPoM configuration has not been studied extensively for the PEC activity. Käll et al. demonstrated at the first time the possibility of application of NPoM systems for PEC water splitting in the visible spectral range using Au as both reflecting mirror and back contact (a continuous Au film) and absorbing material (Au NPs) in the wavelength region of 550–800 nm [34]. Furthermore, all studies published so far utilize exclusively Au as reflecting mirror and absorbing material [39–41], which limits the NPoM systems in real-life applications due to its high cost.

Gold (Au) is the most widely investigated noble metal in the plasmonic field due to its superior chemical and physical stability. A variety of plasmonic nanostructures has been produced by various chemo-physical methods [42,43]. However, the work function of Au is 5.1 eV, which forms a Schottky barrier of ~1 eV with TiO_2 and by that limiting the hot carriers mostly to the intraband excitation [44]. Furthermore, the high cost of Au limits its wide application in the PEC water splitting cells, then Ag and Cu may be considered as alternative plasmonic metals. The main advantage of these metals is that their work functions are smaller than that of Au (4.64–4.75 eV for Ag and 4.65 eV for Cu) [44,45]; therefore, they form a lower Schottky barrier with the TiO_2, which were determined as 0.83 eV for Ag/TiO_2 [46], and 0.63 eV for Cu/TiO_2 interfaces [44]. On the other hand, the interband transition energy levels of these plasmonic metals vary substantially from 2.15 eV for Cu to 2.4 eV for Au, and 4 eV for Ag [44]. Therefore, hot carriers in Ag can only be excited by intraband transitions in the visible range, while in Au and Cu it is possible to generate hot electrons with relatively low energy also by interband excitations [44,47].

In this work, we study a metallic NPs/TiO_2/Ti (NPoM) architecture and demonstrate the possibility to photosensitize a TiO_2 layer sandwiched between metal nanoparticles (either Au, Ag, or Cu) and an underlying reflective metallic Ti mirror. The latter also acts as back contact and electron collector. The TiO_2 layer thicknesses are varied from 20 to 500 nm. We show that such NPoM systems generate multiple resonance peaks within the visible spectral range, *i.e.*, λ = 380–800 nm, due to multiple reflections within the TiO_2 layer resulting in measurable photocurrent. Furthermore, experimental internal quantum efficiency calculations demonstrate at the first time that in Au- and Cu-based NPoMs the hot carriers can be efficiently excited by both intraband and interband electron transitions. At the same time, the Ag-based NPoMs display an asymmetric photocurrent peak at the LSPR band broadened by the constructive interference indicating that the utilization of intraband-exited electrons is amplified in the NPoM configuration even at wavelengths much beyond its plasmonic band. Our results reveal that the mirror component can be considered as an additional degree of freedom in the parameters that influence the efficiency of PEC systems, demonstrating a supplementary route toward the development and optimization of novel and cost-efficient solar energy light-harvesting devices.

2. Results and discussion

2.1. Physicochemical characterization of the NPoM systems

The schematic representation of the NanoParticles-on-Mirror (NPoM) photoelectrochemical system is shown in Fig. 1a. It consists of an e-beam deposited 100-nm-thick reflective metallic Ti layer on a 100-nm-thick SiO_2 on Si substrate effectively preventing light transmission, while the same NPoM systems were also deposited on quartz and glass substrates. These substrates were subsequently covered by a magnetron sputtered TiO_2 layer of various thicknesses. The 3-nm-thick Au layer was then Ar-sputtered on the prepared TiO_2/Ti@SiO_2/Si substrates [30]. The as-deposited noble metal films of this thickness have initially a de-percolated morphology, featuring islands with irregular shapes (Fig. 1b). Such ultrathin films under thermal treatment at certain temperatures, well below their melting point (for Au it occurs at temperatures as low as 200 °C) [48,49], tend to dewet *via* surface diffusion forming well-defined spherical nanoparticles (commonly called islands) [25,30,32]. We had demonstrated previously that such depercolated Au films, deposited on metal oxides, dewet during high-temperature treatment in a matter of minutes in the ambient atmosphere [31]. As-deposited Au films cover the TiO_2 surface by more than 70% (Fig. 1b). While annealed at 450 °C in air, they coalesce displaying the surface coverage of 23 ± 2%, *i.e.*, exposing almost 80% of the TiO_2 surface to PEC reactions (Fig. 1c). The annealed Au NPs have a well-defined round-shaped morphology with a major diameter of 18 ± 8

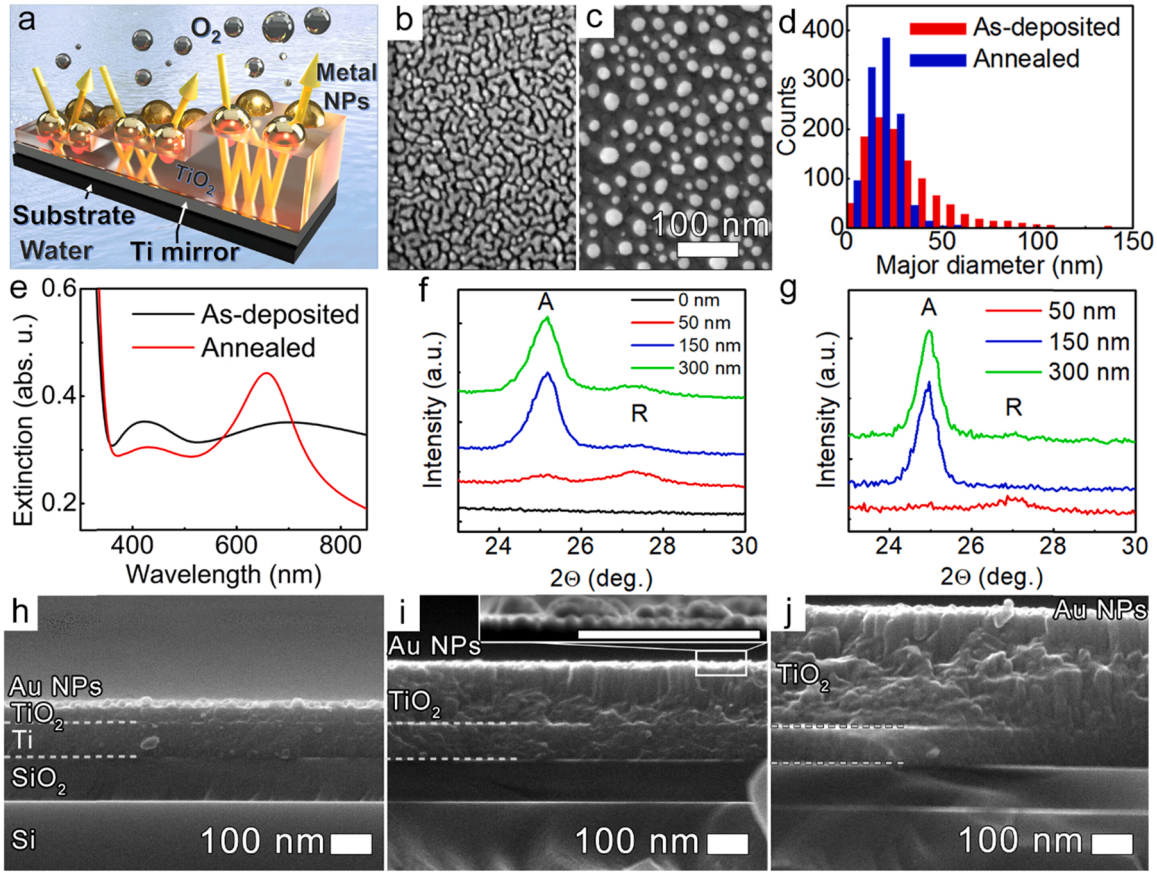

Fig. 1. (a) Schematic representation of the metallic NPs on the mirror approach separated by a thin semiconducting spacer (NPoM). (b-c) Top-view HR-SEM images of (b) as-deposited and (c) annealed Au films deposited on Ti/TiO_2 substrates. (d) Statistical analysis (major NP diameter) of as-deposited and annealed at 450 °C for 5 min in air of 3-nm-thick (nominal mass) Au islands (nanoparticles). (e) Transmittance spectra of 50-nm-thick as-deposited (black line) and annealed at 450 °C for 5 min in air (red line) TiO_2 films on quartz substrates. (f-g) X-ray diffraction of the as-deposited and annealed at 450 °C for 5 min in air TiO_2 films deposited on Si/SiO_2@Ti substrates. (A and R annotate anatase and rutile, respectively). (h-j) Cross-sectional HR-SEM images of the Si/SiO_2@Ti/TiO_2 substrates. The deposited Ti layer thickness is 100 nm, while the TiO_2 layer thicknesses are (b) 50, (c) 150, and (d) 300 nm. The inset image in (i) demonstrates higher magnification of the Au NPs layer on the same NPoM sample. The scale bar is 100 nm.

nm and an aspect ratio of 1.2 ± 0.2 (Fig. 1d). The extinction spectra of the as-deposited and annealed TiO_2/Au NPs layered systems were measured in transmission mode, while prepared directly on quartz substrates (Fig. 1e). The as-deposited Au film on TiO_2 exhibit two bands: (1) the first broadband is located at $\lambda = 425$ nm and associated with the interband transition electrons [34], and the second broadband is located at $\lambda = \sim 700$ nm is related to the localized surface plasmon resonance (LSPR) phenomenon (Fig. 1e) [25]. Once annealed, the shape of the first band remains almost unchanged, while the LSPR band exhibits a significant increase in the optical absorption intensity, a blue shift of ~50 nm in wavelength as well as significant band narrowing due to the narrower NP size distribution and aspect ratio being in good agreement with the published literature [30,50].

The X-ray diffraction spectra in Fig. 1f reveal that the as-deposited TiO_2 is mainly amorphous likely with small crystalline domains of anatase or rutile as evident from the appearance of broad peaks at 25.2° and 27.5° for anatase (JCPDS card No. 21–1272) and rutile (JCPDS card No. 21–1276), respectively, attributed to the (101) anatase and (110) rutile TiO_2 reflections [51]. The gradual transition from rutile-dominated crystalline domains in the thinner TiO_2 layers to anatase-dominated in the thicker deposited layers was observed. Additional XRD measurements (in the 2θ range of 20–80°) confirm the transformation of the TiO_2 films from rutile to anatase phase (Fig. S1a). The metallic Ti bottom layer is observed in the as-deposited samples as evident from the Ti reflection peak at 38° attributed to the (111) reflection (Fig. S1a) [50].

However, thermal treatment in this research is a highly challenging task and should be particularly optimized to avoid excessive oxidation of the underlying metallic Ti layer used as a reflecting mirror from one side, and as a back contact in the PEC setup from another side. Based on our previous experience, the thermal oxidation of the thin metallic films can be followed *in situ* by measuring an optical transmittance using the furnace with the optical path, while plasmonic NPs serve as a transducer (Fig. S2a). This sensing configuration had been found as extremely sensitive, responding immediately to the reactions that occur on the metallic surface due to the oxidation processes, which result in the change of the refractive index in the vicinity to the plasmonic nanoparticles [31]. As shown, during the first 3 min after the exposure of the transducer to thermal treatment, only minor changes in the transmittance are observed (Fig. S2a, blue area), while during the last 2 min the initiation and fast oxidation of the Ti layer occur. The UV–vis spectra measured on the Ti/TiO_2 sample confirm that short time annealing does not change the interference fringe position, *i.e.* the overall TiO_2 thickness remains unchanged, while the intensity changes due to the partial recrystallization of the sputtered TiO_2 layer (Fig. S2b).

The Si/SiO_2, SiO_2/Ti, and Ti/TiO_2 interfaces are clearly observed in the cross-sectional SEM images. Both the SiO_2 and Ti layers are 100-nm-thick, while the thicknesses of the TiO_2 layers vary from 50, to 150, and 300 nm (Fig. 1h–j). The short thermal treatment does not change significantly the polycrystalline nature of the deposited films slightly enhancing the rutile phase in the thinner and anatase phase in the thicker TiO_2 layers (Fig. 1g, and Fig. S1b). The Ti peak at 38° is

overlapping with the (111) reflections of the annealed Au NPs, which display additional peaks at 44.3, 64.5, and 77.7 attributed to the (200), (220), and (311) Au reflections, respectively (Fig. S1b). These results indicate that such a short-time thermal treatment successively preserves the metallic Ti mirror unoxidized yet allows solid-state dewetting of the deposited noble metal films forming plasmonic NPs with well-defined morphology.

2.2. PEC and optical characteristics of NPoMs with TiO_2 layer thicknesses below 50 nm

After light absorption, non-radiative relaxation of NP plasmons can result in the transfer of the incident photon energy to a "hot" electron. Such "hot" electrons can obtain sufficient energy and momentum to overcome the Schottky barrier at the interface between the metal NP and the TiO_2 surface. To measure the photon-to-electron-conversion efficiency, the NPoM architecture was employed as a photoanode in a PEC cell. The schematic diagram of the experiment is illustrated in Fig. 2a. Upon excitation, the electron injection from the metal NPs into the conduction band (or trap states) of the TiO_2 layer occurs leaving a positive charge (hole) on the metal NPs. The holes in the metal NP can further oxidize water molecules in the electrolyte to neutralize the positive charge by accepting electrons [39]. At the same time, electrons injected in the TiO_2 layer can be collected by the mirror that also acts as a back electrical contact. Collected electrons reach the counter Pt electrode, where water reduction takes place. Such an electron flow determines a measurable (photo)-current.

The rutile-dominated 20- and 50-nm-thick TiO_2 layers absorb light in the UV spectral region (<400 nm) due to its wide bandgap demonstrating negligible PEC activity in the visible spectral range [40,50]. Here, the optical bandgap of the TiO_2 films was obtained by Kubelka-Munk equation using UV–vis diffuse reflectance spectra for the indirect allowed transitions ($m = 2$) [52]. While the 20-nm-thick TiO_2 layer exhibits one bandgap at ~3.09 eV ($\lambda = 401$ nm), which corresponds to the amorphous phase of TiO_2 with the mixed rutile/anatase crystalline domains, the 50-nm-thick TiO_2 sample exhibits two band gaps at ~3.45 eV ($\lambda = 360$ nm) and ~1.90 eV ($\lambda = 650$ nm) originates mainly due to optical interference between directly reflected light and the multiple reflections occur at the interfaces of the NPoM configuration (Fig. S3a) [39].

The diffusive reflectance (R) was measured in the wavelength range between 380 and 800 nm covering the complete visible range. The corresponding absorption spectra can be calculated using the following relation: $A + R + T = 100\%$ of the incident light intensity. Since the mirror layer in the NPoM essentially blocks the transmission (T) component within the wavelength range of interest and the diffuse scattering of Au NPs of these sizes is negligible [25,53], the absorbance A can be considered as $A = 100 - R$ [39]. Fig. 2b–c summarizes the experimental results of the NPoM samples with the TiO_2 layer thicknesses up to 50 nm. The samples with 20- and 50-nm-thick TiO_2 layers do not display a pronounced interference pattern. The band in the optical spectra around $\lambda = 650$ nm is attributed to the Au NPs LSPR band, which is in agreement with the literature considering the refractive index of the underlying rutile layer as 2.72 [54], and the refractive index sensitivity of Au NPs of this size as ~70 nm per refractive index unit [55]. Despite differences in the optical spectra, these NPoM samples exhibit one broad IPCE peak at the visible spectral range (Fig. 2b–c, blue spectrum), while in both cases, the photocurrent peak is localized near the LSPR absorption band at $\lambda = 630$ nm and is in agreement with our previous findings [50]. The PEC efficiency depends strictly on the absorption intensity exhibiting maximal values of 0.04% and 0.10% for the 20- and 50-nm-thick TiO_2 NPoM samples in the visible spectral range, respectively (Fig. 2b–c, blue spectra).

We performed several control experiments: (1) the Ti mirror with a thermally grown TiO_2 layer does not exhibit any detectable photocurrent (Fig. S4). (2) The 3-nm-thick Au NPs on the 50-nm-thick TiO_2 layer, deposited directly on a fluorine-doped tin oxide (FTO) glass substrate, *i.e.* no mirror component, exhibits a negligible background photocurrent only (Fig. 2c, dark blue spectrum). The latter results demonstrate a ~20-fold increase in the PEC activity of the NPoM configuration due to the presence of the reflective Ti bottom layer only (Fig. 2c).

2.3. PEC and optical properties of the NPoM systems with TiO_2 layer thicknesses above 50 nm

The situation changes noticeably when the thickness of the TiO_2 layer reaches 75 nm or above. The IPCE response and optical characteristics for the NPoM samples with increasing TiO_2 layer thicknesses *i.e.* 75, 100, 150, 200, 300, and 500 nm were measured and the results are summarized in Fig. 3. As shown, the number of FP interference fringes increases in the spectral range of interest from one (75-nm-thick TiO_2) to two (300-nm-thick TiO_2) and four (500-nm-thick TiO_2). According to the numerical simulations, at the constructive interference maxima wavelengths, a strong localization of the electric field occurs at the Au NP layer (Fig. S5).

TiO_2 layers thicker than 100 nm are mainly composed of anatase crystalline phase, and, therefore, feature a bandgap around 3.2 eV (Fig. S6a). The IPCE data of the NPoM samples demonstrate that the mirror component substantially enhances the efficiency of the "hot" electron generation. Furthermore, the photocurrent in the NPoM samples is not restricted to the LSPR band position but extends to additional wavelength ranges according to the FP cavity resonances development. For instance, the absorbance spectra show one broadband shift from 455 to 550 nm for the 75- and 100-nm-thick TiO_2 samples, respectively. At the same time, the IPCE spectrum reaches its maximum value of ~0.11% for the 75-nm-thick TiO_2 sample at $\lambda = 430$ nm and 0.10% for the 100-nm-thick TiO_2 sample at $\lambda = 565$ nm. These peak wavelengths are 220 and 100 nm blue-shifted compared to the LSPR band of Au NPs

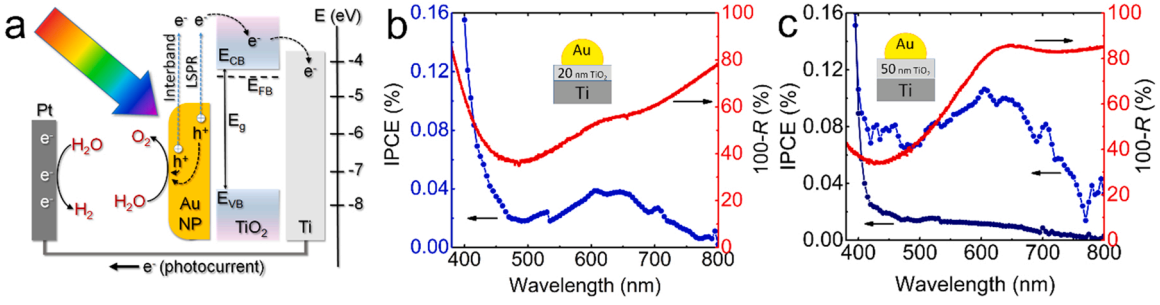

Fig. 2. (a) Schematic diagram of the photoelectrochemical experiment with photon energy smaller than the semiconductor bandgap. (**b-c**) Optical (100% - Reflectance, red spectrum) and corresponding IPCE spectra (blue spectrum) of the NPoM samples of 100-nm-thick Ti film deposited on Si/SiO_2 substrate, followed by the deposition either (b) 20 or (c) 50-nm-thick TiO_2 layer, followed by the deposition of 3-nm-thick Au layer, then annealed 5 min at 450 °C in air. The dark blue spectrum in (c) represents the PEC response of the TiO_2-Au NPs system with the same dimensions deposited directly on a fluorine-doped tin oxide glass substrate.

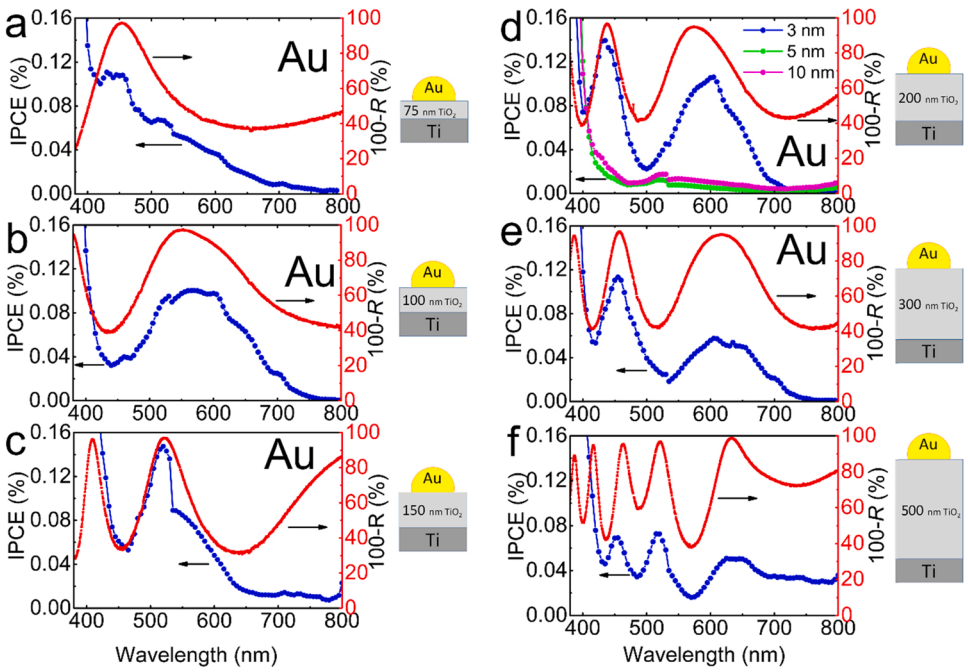

Fig. 3. Schematic representation, optical (100% - Reflectance, red spectrum), and corresponding IPCE spectra (blue spectrum) of the Au- based NPoM samples with various TiO_2 layer thicknesses: (a) 75, (b) 100, (c) 150, (d) 200, and (e) 300. The green and magenta spectra shown in (d) are corresponding to the NPoM samples with 300-nm-thick TiO_2 but subsequently deposited by a 5- or 10-nm-thick Au layer. All samples were annealed for 5 min at 450 °C in air to minimize the Ti mirror oxidation.

(Fig. 3a–b). At the same time, the 150-nm-thick TiO_2 sample shows two interference absorption maxima at $\lambda = 409$ nm and 523 nm, while its relative IPCE spectrum displays one peak at $\lambda = 520$ nm, while the second one that located at $\lambda = 409$ nm overlaps with the TiO_2 bandgap (Fig. S6b).

The 200-nm-thick TiO_2 sample shows two FP interference peaks in the absorbance spectrum at $\lambda = 440$ nm and 575 nm, both are substantially lower in energy compared to the anatase TiO_2 band gap (Fig. 3d, red curve). Here, the relative IPCE spectrum also displays two peaks at $\lambda = 435$ and 604 nm reaching values of 0.14% and 0.11%, respectively. Moreover, the IPCE spectrum shape follows strictly the absorption spectrum displaying a narrower band for the interference peak at $\lambda = 440$ nm and the much broader band for the one at $\lambda = 575$ nm (Fig. 3d, blue curve). It should be noted that the increase in all IPCE values at $\lambda = \sim 525$ nm, and, in particular, clearly observed in the 150-nm-thick TiO_2 sample, occurs due to the filter wheel change in the IPCE station, while in the 150-nm-thick TiO_2 sample it is enhanced by the interference maxima. Therefore, the spectrum of bare Ti/TiO_2 was subtracted in all PEC efficiency calculations.

It was previously reported that the PEC activity of the TiO_2/Au NP photoanodes, *i.e.*, without the mirror component, enables plasmonic PEC water splitting under visible light illumination, with an IPCE maximum value for TiO_2 surfaces decorated by *ca.* 30 nm in diameter Au NPs [40,50,56]. Nonetheless, although optical measurements display a redshift of the LSPR band with the increasing Au NP size, the photocurrent was found to peak at around 600 nm regardless of the Au NP size, *i.e.* the wavelength of maximum photocurrent is size-independent [50]. As was demonstrated, the hot carriers' transport occurs mainly in the ballistic regime, while the contribution of scattered carriers in the larger plasmonic NPs increases only at higher photon energies due to increased distance to the metal-semiconductor interface [57]. Therefore, we examined how various sizes of Au NPs affect the PEC efficiency of the TiO_2/Au NPs layers in the NPoM configuration, *i.e.*, with mirror component. For that, 5- and 10-nm-thick Au layers (nominal mass thickness) were deposited on the 200-nm-thick TiO_2 layer samples, which were subsequently annealed at 450 °C for 5 min in air. The NP size distribution increases from 59 ± 32 nm to 110 ± 64 for 5- and 10-nm-thick deposited Au films, respectively as well as the aspect ratio increases from 1.6 ± 0.6–1.8 ± 0.7 for 5- and 10-nm-thick Au layers, respectively (Fig. S7a–b). The latter is due to the gradual transition of the as-deposited Au layers from initially-depercolated (3-nm-thick) to partially- (5-nm-thick), and almost completely (10-mn-thick) percolated Au films [30]. In the latter cases, the solid-state dewetting of Au films follows a different regime that requires a longer time, while the short-time annealing, used in this study, is unable to accomplish both processes, *i.e.* depercolation by solid-state dewetting, and then coalescence of the dewetted Au NPs (Fig. S7c–d) [30]. The IPCE measurements indicate, however, that the PEC efficiency in the visible spectral range reduced by order-of-magnitude in both cases compared to Au NPs obtained from 3-nm-thick Au films. As discussed by Govorov et al. and Atwater et al., an increase in the noble metal NP size leads to enhanced scattering and decreased rate of generation of hot electrons as well as a longer distance to their migration to reach the semiconductor interface, *i.e.*, increased probability of charge-carrier recombination [57–59]. Furthermore, the reduced fraction of the available three-phase boundary, *i.e.*, the metal/semiconductor/electrolyte junction - the centers where a photoreaction can take place since the enhancement of the electric field is localized at the metal/semiconductor/electrolyte interface upon excitation (see below), may be responsible for the drastic photocurrent decrease [60]. Yet, the IPCE spectra follow the absorbance shape demonstrating two, significantly less-pronounced, IPCE bands (Fig. S7e–f).

The FP interference effect was observed also for the 300-nm-thick TiO_2 sample with a 3-nm-thick Au layer. Here, the NPoM sample exhibits an additional redshift of the interference fringes due to the increase in the spacer thickness appearing at $\lambda = 460$ nm and 620 nm, and the corresponding IPCE spectrum demonstrates two peaks at $\lambda = 455$ nm and 625 nm reaching values of 0.115% and 0.06%, respectively (Fig. 3e).

When the thickness of the TiO_2 layer reaches 500 nm, four interference fringes appear at $\lambda = 415$, 460, 520, and 630 nm (Fig. 3f). At the same time, three IPCE peaks are clearly observed at $\lambda = 450$, 520, and 640 nm, and the shoulder that appears at around 400 nm indicates the overlapping of the fourth peak with the bandgap of TiO_2 (Fig. 3f, blue spectrum). To highlight the presence of the fourth peak, the IPCE spectrum of this sample was subtracted by the one measured without Au NPs (Fig. S8, dark blue spectrum); the fourth peak is thereby clearly observed at $\lambda = 407$ nm (Fig. S8, blue spectrum).

To extend further the PEC activity of the NPoM systems, the subsequent deposition of TiO_2/Au NPs double layers was examined. Here, we compared two NPoM systems. The first system consists of a 100-nm-thick Ti mirror with subsequently deposited 200-nm-thick TiO_2 and 3-nm-thick Au layers, and then annealed at the standard conditions, *i.e.* one shown in Fig. 3d. The optical response as well as the relative IPCE spectrum exhibit two FP interference fringes/peaks at the same wavelengths (Fig. 4a–b, red spectra). The second NPoM system was formed starting from the first one, on top of which an additional layer of 300-nm-thick TiO_2 was sputtered (Si/SiO_2@Ti/TiO_2/AuNPs/TiO_2). The additional 300-nm-thick TiO_2 layer covers completely the first double layer of TiO_2/Au NPs exhibiting negligible photocurrent in the visible light range (Fig. 4b, green spectrum), even though several FP interference fringes are observed from the reflectance spectrum (Fig. S9a–b). Then, the Si/SiO_2@Ti/TiO_2/AuNP/TiO_2 architecture was further coated by an additional 3-nm-thick Au film and annealed (Fig. 4c). The statistical analysis of 1st and 2nd Au NP layers reviles similar size distribution (Fig. 4d–f). However, a substantial increase in the PEC activity in the visible spectral range was observed in this sample featuring three evident IPCE peaks well in line with the optical absorbance spectrum (Fig. 4a–b, blue spectra).

Finally, when the Ti/TiO_2 samples were deposited by a continuous 10-nm-thick Au layer, which covers 99.8% of the top TiO_2 surface, and despite the FP features, negligible photocurrent under visible light illumination was only observed (Fig. S9c–d). These experimental results together with controls further validate that (1) the presence of the metal NPs atop the TiO_2 layer is crucial to transduce the optical characteristics of the NPoMs into visible light photocurrent, (2) the available metal/semiconductor/electrolyte boundary is essential for the PEC activity of the NPoM samples in the visible spectral range, and (3) the PEC activity of the NPoMs in the visible spectral range is determined strictly by FP interference pattern rather than by LSPR peak position of metal NPs.

2.4. PEC and optical properties of NPoM systems with metallic Cu and Ag NP

Au NPs are the most commonly explored plasmonic nanomaterials due to their superior physicochemical features including chemical and thermal stability. However, the high price of Au limits its broad application in the PEC applications. Therefore, we examined other metals as an alternative to Au NPs. Here, Ag or Cu NPs assembled in the NPoM configuration similarly to Au NPs demonstrated comparable PEC responses (Fig. 5). 3-nm-thick Ag or Cu layers were Ar-plasma sputtered then annealed in pure Ar atmosphere at 450 °C for 5 min to avoid their oxidation. As can be seen, the short time annealing is sufficient to dewet these metallic films (Fig. 5b, e). The obtained Ag and Cu NPs are nearly semispherical with the size distribution of 27 ± 14 and 21 ± 15 nm for Ag and Cu NPs, respectively (Fig. 5c, f). However, their (TiO_2) surface coverage is quite different. The dewetted Ag NPs cover ~23% of the TiO_2 top surface, which is comparable to Au-based NPoMs, while Cu NPs cover only ~10% (Fig. 5b, e). The latter indicates that Cu exhibits different wetting/dewetting modes on TiO_2 rather than Au and Ag due, *e.g.*, to their different, melting point, surface diffusion, or substrate wettability, *i.e.*, adsorption energies, as will be discussed below [61,62].

The photocurrent response and optical properties for the Ag- and Cu-based NPoM samples with a 200-nm-thick TiO_2 layer were measured and the results are presented in Fig. 5a, d. The IPCE spectra of both Ag- and Cu-NPoM samples demonstrate that the mirror component existent in these structures substantially enhances the efficiency of hot electron generation. Again, the photocurrent in the Ag- and Cu-based NPoMs is not limited to the LSPR band position, but extends to various wavelength ranges according to the FP interference fringes, and therefore depending on the TiO_2 layer thickness, *i.e.* similar to what was observed in the Au-based NPoMs. Moreover, the tendency in the IPCE spectrum is similar for all the investigated metals, *i.e.*, the IPCE spectrum in all cases has the same number of peaks as the FP interference fringes in the optical absorbance (Figs. 3 and 5a, d).

Interestingly, the IPCE efficiency of the first band, located in the range between 400 and 500 nm, is much higher than the second one located between $\lambda = 500$ and 700 nm, where the LSPR band is expected (Fig. S10a) [25,63]. This even though the optical absorbance is of similar intensity in both interference maxima (Fig. 5a, d). Moreover, the maximum efficiency of the IPCE spectrum of the second (LSPR) band is almost similar, showing a value of ~0.10% for all metals (Fig. 3d, and

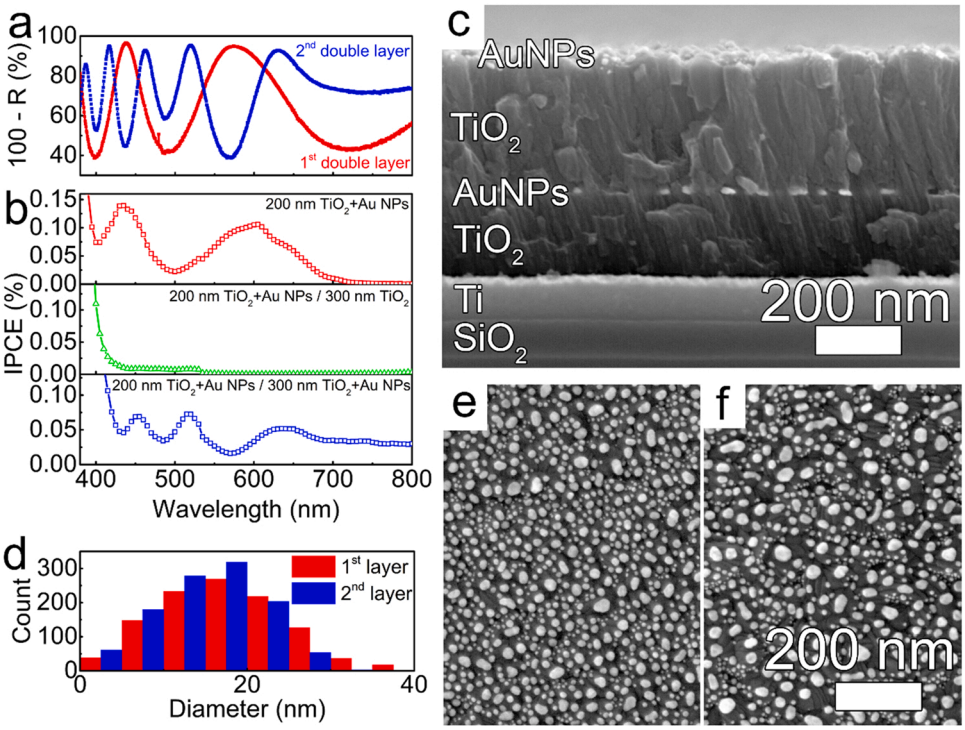

Fig. 4. (a) Optical (100% - Reflectance, full symbol), and (b) corresponding IPCE (open symbol) spectra of subsequently deposited 200-nm-thick TiO_2/Au NPs (red spectra), 200-nm-thick TiO_2 /Au NPs + 300-nm-thick TiO_2 (green spectrum), and 200-nm-thick TiO_2 /Au NPs + 300-nm-thick TiO_2/Au NPs (blue spectra) NPoM samples. (c) Cross-sectional HR-SEM image of the Si/SiO_2@Ti/200nmTiO_2/Au NPs/300nmTiO_2/Au NPs sample. (d) NP size distribution and corresponding (e-f) top-view HR-SEM images of 1st (left image) and 2nd (right image) Au NP films of the NPoM samples with 200- and 500-nm-thick TiO_2 layers, annealed 5 min at 450 °C in air. (For interpretation of the references to colour in this figure, the reader is referred to the web version of this article.)

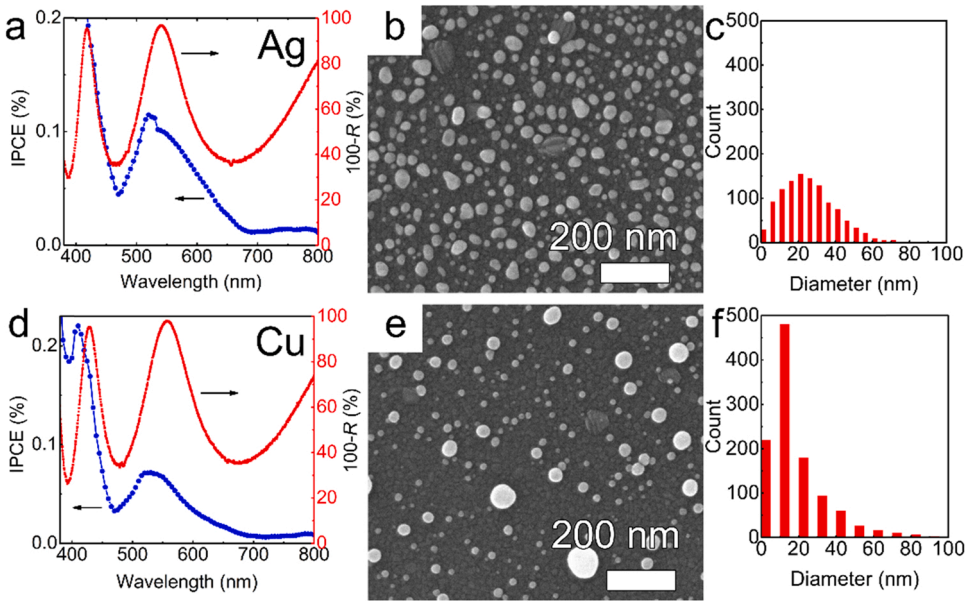

Fig. 5. (a) Optical (100% - Reflectance, red spectrum), and corresponding IPCE spectra (blue spectrum), of the 200-nm-thick TiO_2 NPoM samples with 3-nm-thick Ag (a), or Cu (d) NPs, annealed at 450 °C for 5 min in Ar. (b, e) Top-view HR-SEM images and (c, f) NP size distribution of the Ag NPs (b-c) and Cu NPs (e-f).

5a, d). The intensity of the first IPCE peak, located in the range between 400 and 500 nm, demonstrates higher intensity in the cases of Ag and Cu NPs than the one obtained with Au NPs. This is attributed to the more efficient absorbance of Ag and Cu compared to Au in this spectral region due to the interband transitions in the case of Cu and to the higher plasmonic modes for Ag NPs (Fig. S10b). In both of these cases, the maximal photocurrent efficiency is twice higher than that observed for the peak associated with the LSPR excitation, reaching 0.20% and 0.22% for Ag at $\lambda = 420$ nm and Cu at $\lambda = 409$ nm, respectively. Nevertheless, the IPCE peak at short wavelengths is in all cases higher than that measured near the LSPR band, while the interference maxima have similar absorbance intensity.

2.5. PEC efficiency of NPoM systems in the visible spectral range as a function of applied potential

All of the above observations demonstrate undoubtedly that the PEC efficiency depends strictly on the optical characteristics, *i.e.* the thickness of the TiO_2 layer deposited between the metallic mirror (Ti) and the metal NPs (Au, Ag, or Cu), while the mirror component and the metal NPs are essential to amplify the photocurrent response and to extend it over wavelengths that would otherwise not be absorbed by the metal NPs. Here, we examined the PEC efficiency of the Au-based NPoM system as a function of the applied bias (Fig. 6a–b). As expected, the PEC activity depends strongly on the external potential, as the field drives charge separation and, therefore, affects the charge collection efficiency. All IPCE spectra measured at applied potentials > 0.60 V *vs.* RHE demonstrate similar shape-dependence matching the measured optical absorbance spectrum. The same sample displays significantly lower PEC activity at applied potentials <0.60 V *vs.* RHE, while the measured IPCE spectra barely match the relative absorbance. The flat band (photocurrent onset) potential for the sample was estimated as 0.56 V from *J-V* curve (Fig. 6b, red dotted line).

A significant effect on PEC efficiency as a function of external potential is evident from the photocurrent transient measurements (Fig. 6b). Positive spikes in the current transients were observed immediately after turning the light on at applied potentials below 0.70 V indicating the recombination or trapping of the extracted hot electrons [50]. While larger biases were applied, they afford more driving force to extract, separate and collect the extracted hot electrons resulting in

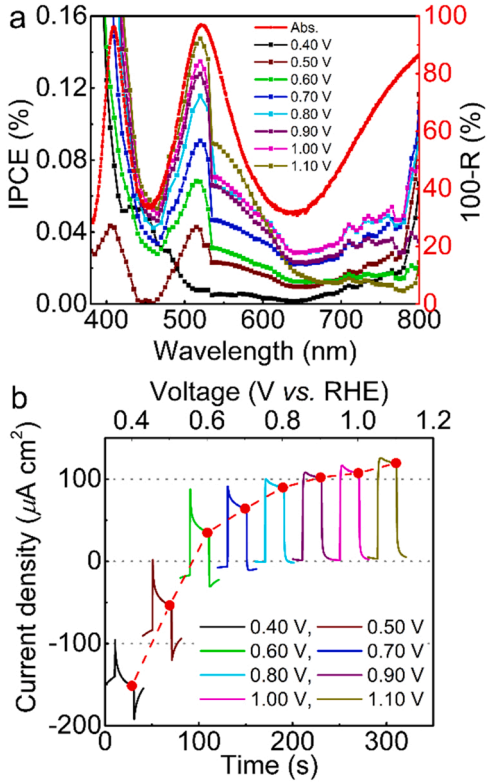

Fig. 6. (a) Optical (100% - Reflectance, red spectrum), and corresponding IPCE spectra of the Au NPoM sample with a 150-nm-thick TiO_2 layer measured at various applied potentials. The applied bias is displayed *vs.* the RHE reference electrode. The sharp increase in the IPCE values at $\lambda = \sim 525$ nm occurs due to the filter wheel change in the IPCE station. (b) Chopped light photocurrent-voltage curves of the 150-nm-thick TiO_2 Au-based NPoM system in regular electrolyte solutions measured at $\lambda = 520$ nm. Measurements were performed at voltages in the range from 0.40 to 1.10 V (*vs.* RHE, the voltage difference between each transient is 0.10 V). The red dotted line indicates the photocurrent onset. (For interpretation of the references to colour in this figure, the reader is referred to the web version of this article.)

smaller or no spikes to observe (Fig. 6b). Negative spikes in the current transients upon turning the light off (emptying of states in the dark), were observed at potentials below 0.60 V, whereas above 0.80 V both saturation of the photocurrent and vanishing of the negative spikes occur. At potentials above 0.80 V, the recombination is suppressed due to a complete depletion of electrons within the material [64], *i.e.*, the water splitting in such NPoM systems may occur at the applied potential as low as 0.80 V.

2.6. Factors that affect the PEC activity of the NPoMs

The increased surface roughness (due to increased TiO_2 layer thickness) as well as the affinity of various metals to the TiO_2 substrate affect the dewetting/coalescence processes leading to the formation of an unequal number of NPs per specific surface area as well as broaden NPs size distribution. Therefore, the experimental PEC efficiencies were normalized to the perimeter-per-area-fraction to identify the key factors that may affect the overall PEC efficiency of the NPoM systems in the visible spectral range. The overall PEC efficiency was obtained by integrating the IPCE spectrum over the visible spectral range, *i.e.*, from $\lambda = 380$–800 nm.

First, it should be noted that the wetting of the TiO_2 differs substantially by the NP origin. Fig. 7a–c demonstrates cross-sectional HR-SEM images of Ag, Au, and Cu NPs deposited on the TiO_2 then annealed. As can one observe, the contact angle increases from ~ 72° for Ag, ~ 95° for Au, then rises to ~140° for Cu NPs. The latter can explain the substantial difference in the surface coverage of Ag and Au NPs, which are ~20–25%, while Cu NPs cover only ~10% of the TiO_2 surface. Hence, the overall perimeter and, substantially, the contact area between the metallic NPs and underlying TiO_2, calculated from the top-view SEM images, fits well Ag and Au NPs but were corrected in the case of Cu NPs. It was shown previously, that the contact area between NP and the underlying semiconducting layer is responsible for the increased PEC activity [65] since the hot electron injection efficiency is determined by

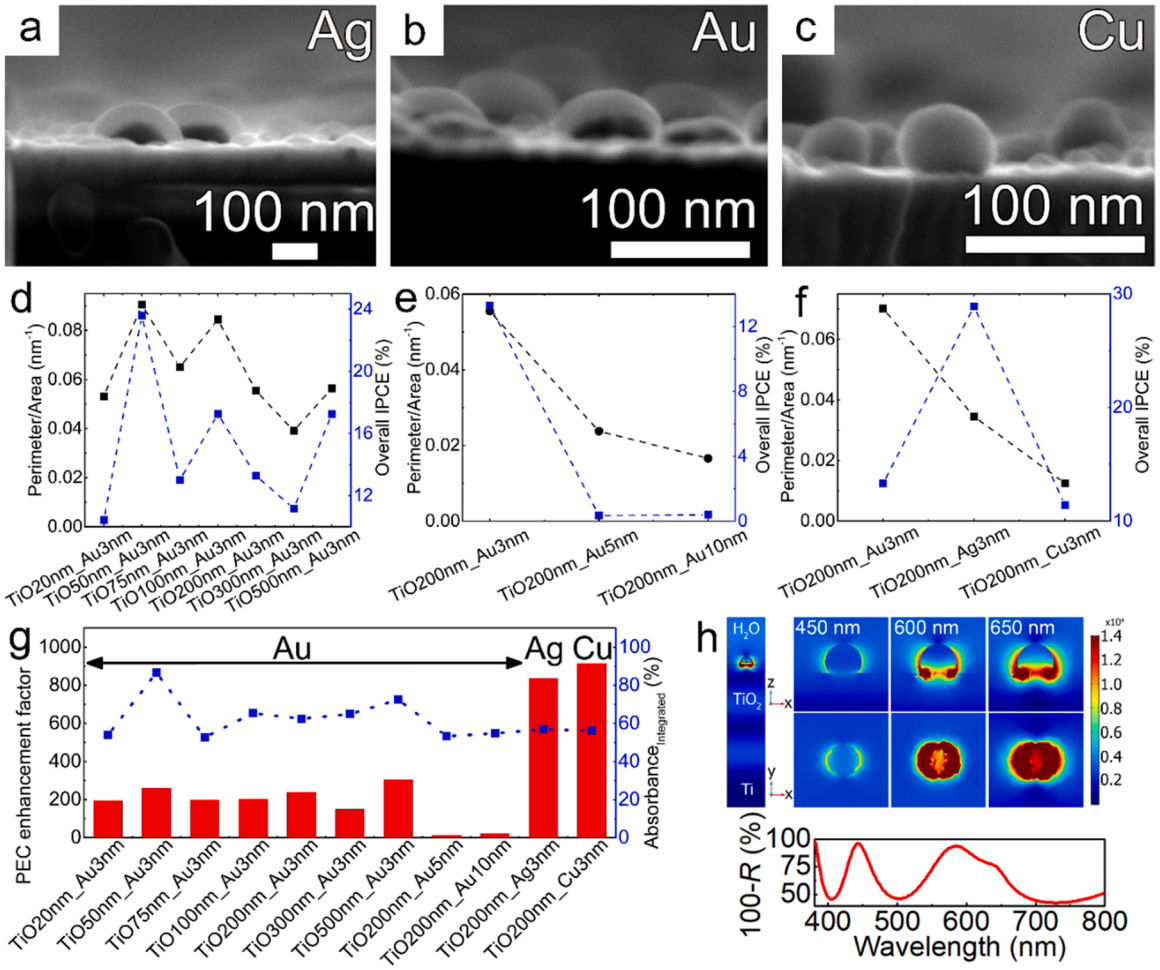

Fig. 7. Cross-sectional HR-SEM images of 3-nm-thick (nominal mass) (a) Ag, (b) Au, and (c) Cu NPs deposited on the TiO_2 layer and annealed. The perimeter of NPs per surface area and integrated IPCE efficiency over the visible spectral range (380 – 800 nm) as a function of (d) TiO_2 thickness, (e) nominal deposited Au thickness, (f) nature of NPs (Au, Ag, or Cu), and (g) The enhancement PEC factor: the integrated IPCE to NP perimeter/area ratio over the visible spectral range. The blue line corresponds to the total absorption integrated from 380 nm to 800 nm wavelengths of the samples used to measure the IPCE. (h) Numerical simulations of the Au-based 200-nm-thick TiO_2 NPoM sample display the electromagnetic field enhancement at the interference maxima $\lambda = 450$ and 600 nm and the LSPR band at $\lambda = 650$ nm. The overall perimeter, *i.e.*, the perimeter of all metallic NPs per predefined area, was calculated from the top-view HR-SEM images and was corrected following the measured contact angle values. Before integrating the IPCE spectrum in the visible spectral range, the IPCE spectrum of the bare Ti-TiO_2 control sample was subtracted. The effect of the increased thickness of the TiO_2 layer was compared using the 3-nm-thick Au NPs (Fig. 7d). The 23.59% overall integrated IPCE value was achieved for the sample with a 50-nm-thick TiO_2 layer, while both 100- and 500-nm-thick TiO_2 samples demonstrate a 17.26% value in the visible spectral range (Fig. 7d, blue line). However, the overall number of NPs within the given area (perimeter-to-area ratio) varies for all NPoM samples due to the different roughness of the deposited TiO_2 layer (Fig. 7d, black line); therefore, we normalized the integrated IPCE values to the perimeter-to-area ratio. As can be seen from the normalized data, the most efficient Au-based NPoM system is a 500-nm-thick TiO_2 sample that shows an enhancement factor of 306, while the 50- and 100-nm-thick TiO_2 samples show the enhancement factors of 261 and 204, respectively.

the energy-momentum distribution of the hot electron population resulting from Landau damping of plasmons [39,57].

The effect of the NPs size, which rises substantially with the increase in the nominal mass deposition Au layer thickness, was examined using the 200-nm-thick TiO_2 NPoM samples and the results are presented in Fig. 7e. It is clear that the overall perimeter decreases drastically with the increase in the nominal Au layer thickness, while the overall NP surface coverage remains almost constant changing from 23% in the 3-nm-thick to 28% and 25% in the annealed 5- and 10-nm-thick Au layers, respectively. At the same time, a strong decrease was observed in the integrated IPCE efficiency. While the 3-nm-thick Au-based NPoM sample exhibits 13.29% integrated PEC efficiency in the visible spectral range, both 5- and 10-nm-thick Au NPoM samples almost vanish exhibiting PEC efficiencies of 0.34% and 0.39%, respectively. The latter indicates that the PEC efficiency is driven not only by the NP size but mainly by the available semiconductor metal catalyst three-phase (Au NP/TiO_2/electrolyte) boundary [60,66]. Finite element numerical simulations verify that the enhancement of the electric field is localized at the metal/semiconductor/electrolyte boundary upon excitation (Fig. 7h, and Figs. S11–13), being in good agreement with the published literature [57,60].

Finally, the effect of the deposited metallic NP origin on the overall PEC efficiency in the visible spectral range was examined (Fig. 7f). Here, 3-nm-thick either Ag or Cu were deposited on the 200-nm-thick TiO_2 NPoM samples then annealed in pure Ar. The perimeter per area ratio decreases exhibiting 0.055 nm^{-1} value for Au NP, then drops to 0.034 nm^{-1} and 0.012 nm^{-1} for Ag and Cu NPs, respectively (Fig. 7f, black line). Among the tested metals, the Ag-based NPoM sample shows the highest integrated IPCE efficiency reaching 28.89% in the visible spectral range, and the Cu-based NPoM sample exhibits the lowest IPCE efficiency displaying 11.41% only (Fig. 7 f, blue line). However, when normalized, Cu- and Ag-based NPoM samples show the enhancement factors, *i.e.*, PEC efficiency of the NPoM system per unit length of triple point boundary, of 915 and 837, respectively. These values are ~ 3-fold higher than the one obtained for the best Au-based NPoM sample, *i.e.*, 3-nm-thick Au NPs deposited on 500-nm-thick TiO_2 layer (Fig. 7g). In other words, Cu and Ag NPoM systems can split water 3 times more efficiently than their Au analogs in the visible spectral range concerning that the available triple point boundary is similar. The latter indicates that even though the overall absorbance, *i.e.*, integrated into the range from $\lambda = 380–800$ nm is nearly similar, the PEC efficiency of the Ag- and Cu-based NPoMs is advantageous between all tested metals (Fig. 7 g, blue dotted line). Here, the enhanced efficiency of Cu-based NPoMs can be attributed to the combined effect of (*i*) lower work function, *i.e.*, the Schottky barrier for hot electrons transfer is reduced to 0.65 eV, (*ii*) lower interband transition energy, which leads to more efficient hot electron extraction [44], and (*iii*) enhanced absorbance at the interference maxima due to strong localization of the electric field at the NP layer. The enhanced efficiency of the Ag-based NPoMs can be also attributed to the combined effect of (*i*) lower work function, while in this case, only intraband excitation can contribute to hot carriers since the interband threshold of Ag is located above 4 eV [67], and (*ii*) strong localization of the electric field at the NP layer.

2.7. The internal quantum efficiency of the NPoM systems

The measured IPCE signal reflects efficiencies for three fundamental processes involved in PEC activity: (*i*) photon absorptance (the fraction of electron/hole pairs generated per incident photon flux), (*ii*) charge transport to the solid-liquid interface, and (*iii*) the efficiency of interfacial charge transfer *i.e.* injection (into the TiO_2 layer) of hot carriers with appropriate momentum and sufficient kinetic energy to overcome the interfacial (metal-TiO_2) Schottky barrier [2]. However, the PEC efficiency measured by IPCE implicitly also includes losses from impinging photons that are reflected and/or transmitted. Therefore, to understand the inherent performance of a material and to determine the optimum balance between maximal path length for photon absorption *vs.* minimal effective transport distance, such losses should be subtracted, provide efficiency values based on the photon flux actually absorbed [68]. This is known as internal quantum efficiency (IQE), which is given by the ratio between the photo-electrochemical (IPCE) and optical (Absorption) performances that contribute to the photocurrent [57]. As expected, all Au-based NPoM samples with various TiO_2 layer thicknesses exhibit characteristic IQE peak around $\lambda = 650$ nm, which is corresponding to the surface plasmon hot carriers excited by intraband electrons (Fig. 8a). At the same time, these NPoM samples exhibit diverse behavior at shorter wavelengths due to a more efficient light trapping within the TiO_2 layer due to FP interference – the latter yields a higher probability of electronic excitation at constructive maxima. Here, the PEC activity can be explained by photoexcited carriers in Au NPs generated primarily from interband transitions by excitation of the *d*-band electrons – the bare TiO_2 substrate does not show any PEC activity in this (visible light) spectral region (Fig. S9) [69]. Fig. 8a also includes a fit of the *IQE* data to the modified phenomenological Fowler model based on a semiclassical model of hot electrons emitted over an energetic barrier [34,70]. This approximation is a common way to compare photovoltaic devices; however, the model accounts exclusively for intraband transitions [57]. The Au-based NPoMs follow Fowler behavior in the range above the interband threshold (1.8 eV ($\lambda = 688$ nm) for Au), while below that, all NPoM samples deviate significantly from that model.

To emphasize the difference in the photo-electrochemical performance, we measured linear polarization resistance (R_{LP}) of the Au-based 300-nm-thick TiO_2 NPoM sample with and without deposited Au NPs as a function of the monochromatic light illumination in a PEC cell in the 0.4 M Na_2SO_4 electrolyte. The 300-nm-thick TiO_2 NPoM sample was chosen because its absorbance spectrum displays several interference maxima/minima far away from the band gap of TiO_2. The R_{LP} was measured at discrete wavelengths using dedicated LEDs with a low spectral half-width: near the wavelengths of constructive ($\lambda = 452$ and 627 nm) and destructive ($\lambda = 510$ nm) FP interference, close to the TiO_2 bandgap ($\lambda = 409$ nm), and much beyond the LSPR band ($\lambda = 774$ nm) (Fig. 8c, green triangles). The resistance of a control sample without Au NPs remains almost constant throughout the visible spectral range displaying values around 60 MΩ cm^{-2} and dropping substantially near the TiO_2 bandgap, where absorption of photons <409 nm generates a high density of charge carriers (Fig. 8d, black points). On the contrary, the resistance of the NPoM sample (Si/SiO_2@Ti/TiO_2/AuNPs) is noticeably different (Fig. 8d, blue points). At longer wavelengths, *i.e.*, far from both the TiO_2 bandgap and the LSPR band of Au NPs, the NPoM sample demonstrates a maximal resistance value of 4.45 MΩ cm^{-2}, which is one order-of-magnitude lower than the control sample without Au NPs. Furthermore, the R_{LP} drops substantially at the first ($\lambda = 627$ nm) and second ($\lambda = 452$ nm) FP constructive interference maxima displaying values of 0.81 and 0.51 MΩ cm^{-2}, respectively. These values are one order-of-magnitude lower compared to the resistance measured for the same sample at $\lambda = 774$ nm, are ~20-fold lower than the resistance measured in the dark (10.90 MΩ cm^{-2}), and are two orders-of-magnitude lower than the resistance measured for the control sample without Au NPs under similar conditions. At the same time, the sample exhibits resistance of 1.28 MΩ cm^{-2} at $\lambda = 510$ nm, *i.e.*, at a wavelength of destructive FP interference (cavity). The lowest resistance of 0.43 MΩ cm^{-2} was obtained again at $\lambda = 409$ nm, *i.e.*, near the bandgap of anatase TiO_2 similar to the control sample. Correspondingly, open circuit potential (OCP) measurements demonstrate that in the dark and under illumination at $\lambda = 774$ nm, *i.e.* far from the LSPR band, the Au-based NPoM sample display OCP of −205 and −175 mV, respectively. At the FP interference maxima points, *i.e.* $\lambda = 452$ and 627 nm, the OCP reduces to −31 and −10 mV, respectively, while increases to −75 mV at $\lambda = 510$ nm, *i.e.* the interference cavity. These results indicate that the illumination of light at particular wavelengths lowers the effective Schottky barrier pushing the hot electrons toward TiO_2 thus making the electrolyte interface more positive facilitating the water-splitting

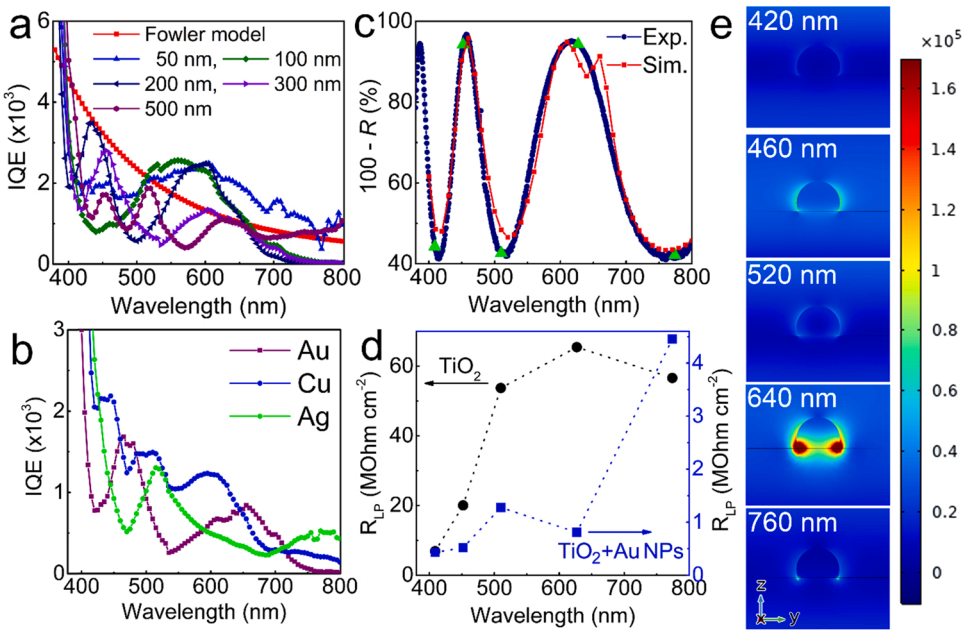

Fig. 8. (a) Calculated IQE from experiment and the phenomenological modified Fowler equation (red spectrum) for (a) the Au-based NPoMs. (b) Calculated IQE for the 200-nm-thick TiO_2 NPoM samples deposited by Au, Ag, or Cu NPs. (c) Experimental and finite elements simulated optical (100% - Reflectance) spectrum of the 3-nm-thick Au-based NPoM sample with a 300 nm-thick TiO_2 layer. (d) Linear polarization resistance measured on the sample shown in (c) with and without subsequent deposition of Au NPs under the illumination of the monochromatic light with $\lambda = 409$, 452, 510, 627, and 774 nm (red points in (c)). (e) Finite elements numerical simulations of the Au-based 300-nm-thick TiO_2 NPoM sample display the electromagnetic field enhancement at green points shown in (c). The images display Au NP-TiO_2 slab immersed in water. (For interpretation of the references to colour in this figure, the reader is referred to the web version of this article.)

reactions. These measurements as well as the numerical simulations, as shown in Fig. 8e**,** imply that the geometry of the NPoM system, mainly in terms of TiO_2 layer thickness but also in terms of Au NP size to a lower extent, primarily dictates their optical properties affecting the transport characteristics of such heterostructured systems. In this sense, the optical profile dictated by FP interference may be considered as an additional degree of freedom in the PEC enhancement processes to the intrinsic material properties such as the metal origin, semiconductor, and barrier height at a metal-semiconductor interface (Fig. 8**d,** and Fig. S11).

The *IQE* spectra of Cu- and Ag-based NPoMs were also calculated. The absorbance spectrum of Cu NPs is comparable to the Au in the wavelength range between 600 and 800 nm but the absorbance of light by Cu NPs is higher in the shorter wavelengths (Fig. S10). Similarly to the Au-based NPoMs, Cu-based NPoM samples exhibit a characteristic *IQE* peak around $\lambda = 650$ nm ascribed to the generation of surface plasmon hot carriers (Fig. 8b), and an additional broad shoulder between $\lambda = 430$–600 nm due to the interband excited electrons, which can be injected into the TiO_2 layer due to the reduced Schottky barrier. Moreover, the *IQE* spectra of the Cu-based NPoM sample shows also PEC activity at $\lambda > 700$ nm corresponding to the increase in the absorbance intensity due to the FP interference (Fig. S12). At the same time, the *IQE* spectrum of the Ag-based NPoMs shows an asymmetric band with the peak at $\lambda = 520$ nm that is attributed to the LSPR excitation of Ag NPs (Fig. S10b), while a long shoulder at $\lambda = 550$–700 nm can only be attributed to the constructive interference field enhancement since the LSPR band of Ag NPs is narrow. Similar to Cu-based NPoMs, there is an additional increase in the IQE efficiency at $\lambda > 700$ nm, which again can be only attributed to the increased absorbance intensity due to the thin-film interference phenomenon (Fig. S13). The latter is of particular interest since it demonstrates that the utilization of intraband-excited electrons can be significantly amplified in the NPoM configuration even at wavelengths much beyond the semiconductor bandgap and plasmonic band of metallic NPs due to constructive reflections from a metallic mirror (Figs. 8b, 5a, and Fig. S13).

3. Conclusion

Herein we developed photoelectrochemical NanoParticles-on-Mirror (NPoM) systems, which consist of a reflective Ti mirror and metallic NPs separated by semiconducting TiO_2 layers with thicknesses varying from 20 to 500 nm. The optical spectra of such samples follow the typical Fabry-P é rot (FP) interference patterns and vary according to their thickness, *i.e.* the number of FP interference fringes increases from one to four in the visible spectral range (380–800 nm) with increasing the TiO_2 layer thickness. We observed that the photocurrent, ascribed to charge carriers photogenerated in such NPoM systems, is substantially amplified in the visible spectral range due to reflections from a metallic mirror and the presence of metal NPs at the TiO_2 surface. The incident photon-to-electron conversion efficiency (IPCE, *i.e.* external quantum efficiency) spectra of such NPoM systems demonstrate solar PEC water splitting in the visible spectral range matching almost completely the absorbance spectra and exhibiting the identical number of fringes even at the spectral regions located much beyond the LSPR band. This can be explained by (***i***) intraband excitation of *s* electrons, and (***ii***) by interband transitions of the *d*-band electrons both can overcome the Schottky barrier due to the reduced resistivity of the NPoM systems at the constructive maxima and even at destructive minima compared to the dark state measurements. However, either missing one component in the NPoM configuration, an increase in the NP size, or a significant decrease in the exposed TiO_2 area fraction result in substantial damping or even complete vanishing in the PEC activity of the NPoM systems in the visible spectral range.

Interestingly, the wetting of the TiO_2 surface by the noble metals used in this study varies substantially influencing the amount of metal NPs per specific area meaning that perimeter-to-area fraction is considerably different in all tested metallic NPs. Therefore, the normalized PEC enhancement factor was calculated by integrating the IPCE spectra in the visible spectral range, which was further divided by the available perimeter-to-area fraction indicating PEC efficiency per available unit triple point boundary of NPs. Among tested NPoM systems, the highest PEC enhancement factor was obtained for the Cu-based NPoM samples, while Ag-based NPoM demonstrates slightly lower efficiency, yet both are ~3-fold greater than the highest value obtained for the Au-based NPoM system. Furthermore, to understand the inherent performance of a material and to determine the optimum balance between maximal path length for photon absorption, internal quantum efficiency (*IQE*) was calculated. The *IQE* spectra show a static LSPR band for all Au-based NPoM samples corresponding to the plasmonic electron excitation, while deviate significantly at shorter wavelengths. In all cases, the NPoM samples exhibit absorbance-dependent behavior in which peaks appear as a function of the FP interference

dictated by the TiO_2 layer thickness.

Our results demonstrate a new paradigm toward the development of novel and cost-efficient solar energy harvesting devices in the visible spectral range. The proposed here NPoM systems based on Ti mirror and Ag or Cu metallic NPs demonstrate similar order of magnitude in their PEC activity as their Au-based NPoM analogs published in the literature [34,39,41], while demonstrating 2 orders-of-magnitude lower cost. Still, several improvements and optimization of the light-harvesting device should be further examined from the material and architectural points of view. For instance, an efficient annealing profile should be developed to improve the crystallinity of the semiconductor layer, bandgap engineering of the semiconductor to enhance its electron mobility, the extent of the NPoM approach to non-noble metals as well as the development of processes to increase the interfacial area between metallic NP and a semiconductor (2D and 3D architectures), and an increase in NPs surface coverage (in the case of high enough NP density to produce electromagnetic hot spots). In all these cases, the enhanced PEC efficiency is expected, while the underlying mirror will further expand and amplify the overall system PEC efficiency.

4. Experimental section

4.1. Deposition of Ti films

Before Ti deposition, the Si/SiO_2 substrates (SiO_2/Si; 3 in., μChemicals, Si(100) p-type + 100 nm SiO_2) were cleaned ultrasonically in acetone, ethanol, and deionized water (10 min for each step), then dried under an N_2 stream. The Ti metal coating was e-beam evaporated from a Ti target (Hauner HMW, 99.999%) operated in a direct current mode, with a deposition power of 150 W, at room temperature. During the deposition, the working pressure was held constant at 1×10^{-3} mbar and the Ti metal deposition time was ~10 min, forming a Ti metal film with a thickness of 100 nm.

4.2. Deposition of Ti-TiO_2 films

The TiO_2 films of various thicknesses from 5 to 500 nm were produced by reactive magnetron sputtering in an ultrahigh vacuum chamber (Createc, SP-P-US-6 M-3Z) on a 100-nm-thick Ti metal-coated SiO_2/Si wafers. Control experiments were carried out by producing the TiO_2 surfaces also on other Ti-coated substrates such as quartz slides (GBV, Germany) and directly on quartz slides for transmittance measurements.

4.3. Deposition of metallic nanoparticles

The deposition of metal NPs was carried out by solid-state dewetting of thin metal films. First, ultrathin layers of Au, Cu, or Ag on the TiO_2 were carried out using a high vacuum Ar-plasma sputtering machine (Leica - EM SCD500). The nominal thickness for Ag and Cu films was 3 nm (determined *via* QCM). Besides, some control Au films were also sputtered with a thickness of 5 and 10 nm. The pressure of the sputtering chamber was reduced to 10^{-4} mbar and then set at 10^{-2} mbar of Ar. The applied current was 16 mA resulting in an average deposition rate of ~0.1 nm/s. An automated quartz crystal microbalance monitor determined the amount of sputtered metal. The Au-coated TiO_2 surfaces were annealed in a pre-heated tubular furnace for 5 min at 450 °C in air. The Ag- and Cu-coated TiO_2 substrates were annealed in a pre-heated tubular furnace for 5 min at 450 °C in Ar atmosphere, purged with Ar for 30 min before and after the thermal treatment. Statistical analysis of the metal NPs was performed on HR-SEM images of as-deposited and annealed metal films using the ImageJ software.

4.4. Surface morphology and physicochemical characterization

For morphological characterization, a field-emission scanning electron microscope (Hitachi FE-SEM S4800) was used. X-ray diffraction analysis (XRD, X′pert Philips MPD with a Panalytical X′celerator detector) using graphite monochromized Cu Kα radiation (wavelength 1.54056 Å) was used for determining the crystallographic composition of the samples. The composition and the chemical state of the films were characterized using X-ray photoelectron spectroscopy (XPS, PHI 5600, US), and the spectra were shifted according to the C 1 s signal at 284.8 eV, and peaks were fitted with Multipak software.

4.5. Optical measurements

Diffusive reflectance spectra at the different preparation steps were measured by a fiber-based UV–vis-IR spectrophotometer (Avantes, ULS2048) equipped with an integrating sphere AvaSphere-30 using AvaLight-DH-S-BAL balanced power light source. The transmission measurements were performed on TiO_2/Me NPs (Me = Au, Ag, or Cu) films deposited on quartz substrates using a double-beam UV–vis spectrometer (Perkin-Elmer Lambda 950) with an illumination beam of approximately 8 mm in diameter from 300 to 1000 nm with 2 nm resolution.

4.6. Photoelectrochemical measurements

Incident photon-to-electron conversion efficiency (IPCE) measurements were carried out in the 300–800 nm range with a setup comprising an Oriel 6356 150 W Xe arc lamp as the light source and an Oriel cornerstone 7400 1/8 monochromator. The spectra were recorded by measuring the photocurrent transients (20–10 s light on-off cycles) under monochromatic illumination with a λ step-size of 5 nm and under a defined external electric bias. The setup is equipped with different cut-off filters automatically arranged in the following configuration: when measuring at λ from 800 to 590 nm, a filter is activated that cuts off photons with $\lambda < 450$ nm; when measuring at λ from 590 to 360 nm, the filter is switched over to another one that cuts off photons with $\lambda < 300$ nm. The measurements were carried out in as-prepared aqueous 0.4 M Na_2SO_4 solutions (pH = 6.84), in most of the experiments at an applied potential of 500 mV (*vs.* $Ag/AgCl_{Sat}$), in an electrochemical cell equipped with a quartz window (area = 1 cm^2) and operated in a three-electrode configuration with the NPoM sample used as a working electrode, an $Ag/AgCl_{Sat}$ electrode as the reference electrode, and a Pt foil as the counter electrode. The measured potentials *vs.* Ag/AgCl were converted to the reversible hydrogen electrode (RHE) scale according to the Nernst equation: $E_{RHE} = E_{Ag/AgCl} + 0.059\ pH + E^o_{Ag/AgCl}$, where E_{RHE} is the converted potential *vs.* RHE, $E^o_{Ag/AgCl} = 0.1976$ at 25 °C, and $E_{Ag/AgCl}$ is the experimentally measured potential against Ag/AgCl reference.

4.7. Linear polarization resistance (R_{LP}) measurements

The linear polarization resistance measurements were performed using a Zahner IM6ex (Zahner Elektrik, Kronach, Germany) photoelectrochemical workstation equipped with CIMPS QE/IPCE TLS03 tunable light source. The experiments were conducted either in the dark or under illumination provided by monochromatic sources (LED-based light) in a 0.4 M Na_2SO_4 aqueous electrolyte. A three-electrode cell with Pt as a counter electrode, the 200-nm-thick NPoM sample as a working electrode, and $Ag/AgCl_{Sat}$ as a reference electrode were employed. The R_{LP} was measured at discrete wavelengths: λ = 409, 452, 510, 627, and 774 nm with the same power density of 4.15 mW cm^{-2}. The R_{LP} was measured in the interval of ± 10 mV *vs.* open circuit potential (OCP) with a scan rate of 0.2 mV s^{-1}.

4.8. Internal quantum efficiency (IQE) calculations

The experimental internal quantum efficiency was obtained as follows: the TiO_2 layers with subsequently sputtered 3-nm-thick metallic NPs were deposited on quartz substrates, and then annealed either in air or in Ar atmosphere. The transmittance and reflectance signals were

measured using a double-beam UV–vis spectrometer (Perkin-Elmer Lambda 950) with an illumination beam of approximately 8 mm in width from 300 to 1000 nm with 2 nm resolution equipped with an integrating sphere. In such a configuration, the transmittance spectrum includes the absorption and scattering components, while the reflectance spectrum consists of scattering only. The absorbance spectrum was obtained by subtraction of reflectance from the transmittance spectrum. The experimental IPCE spectrum of NPoMs was first subtracted by the Ti/TiO_2 IPCE spectrum to remove spike that occurs due to the optical filter switch in the IPCE measuring device, then these spectra were divided by the spectrum acquired from the absorbance calculations to obtain the IQE. We calculated the IQE using the optical data obtained from the sample without the mirror component since the total absorbance is directly proportional to the absorbance in the metallic NP.

4.9. Numerical simulations

A commercial software COMSOL Multiphysics was used for all-optical simulations based on a finite element method. The Au particles were modeled as spherical with 30 nm in diameter on the TiO_2 layer, truncated at 40%, with various thicknesses and 100-nm-thick Ti film. The surrounding medium was water. We used periodic and port boundary conditions in the horizontal and vertical directions, respectively. The excitation light was linearly polarized and incident from the waterside of the sample. For Au, Cu, Ag, anatase, and rutile TiO_2, and metallic Ti, dispersive dielectric constants from the literature were used [71,72].

CRediT authorship contribution statement

A.B.T., M.A., and S.H. synthesized the photoanodes. A.B.T, T.S., R. M., and N.V. performed the numerical optical simulations. The photoanodes were characterized and analyzed by A.B.T. and M.A. for photoelectrochemistry, HR-SEM, XPS and XRD. A.B.T. wrote the draft with the help of M.A. and P.S. This work was initiated by A.B.T. and P.S. P.S. supervised the project.

Declaration of Competing Interest

The authors declare that they have no known competing financial interests or personal relationships that could have appeared to influence the work reported in this paper.

Acknowledgements

The authors acknowledge the DFG and DFG Cluster of Excellence Engineering of Advanced Materials (EAM) for financial support. A.B.T would like to acknowledge the Emerging Talents Initiative (ETI) of Friedrich-Alexander University, Germany, grant number 5500102, and the DFG (grant number 442826449; SCHM 1597/38-1 and FA 336/13-1) for financial support. We thank Dr. A.V. Solomonov for discussion and design of graphical table of content.

Appendix A. Supporting information

Supplementary data associated with this article can be found in the online version at doi:10.1016/j.nanoen.2021.106609.

References

[1] A. Fujishima, K. Honda, Electrochemical photolysis of water at a semiconductor electrode, Nature 238 (5358) (1972) 37–38.
[2] C. Jiang, S.J.A. Moniz, A. Wang, T. Zhang, J. Tang, Photoelectrochemical devices for solar water splitting – materials and challenges, Chem. Soc. Rev. 46 (15) (2017) 4645–4660.
[3] M.G. Walter, E.L. Warren, J.R. McKone, S.W. Boettcher, Q. Mi, E.A. Santori, N. S. Lewis, Solar water splitting cells, Chem. Rev. 110 (11) (2010) 6446–6473.
[4] C. Liu, B.C. Colón, M. Ziesack, P.A. Silver, D.G. Nocera, Water splitting–biosynthetic system with CO_2 reduction efficiencies exceeding photosynthesis, Science 352 (6290) (2016) 1210–1213.
[5] S. Sun, J. Zhang, P. Gao, Y. Wang, X. Li, T. Wu, Y. Wang, Y. Chen, P. Yang, Full visible-light absorption of TiO2 nanotubes induced by anionic S22− doping and their greatly enhanced photocatalytic hydrogen production abilities, Appl. Catal. B 206 (2017) 168–174.
[6] A. Hagfeldt, G. Boschloo, L. Sun, L. Kloo, H. Pettersson, Dye-sensitized solar cells, Chem. Rev. 110 (11) (2010) 6595–6663.
[7] P.K. Nayak, S. Mahesh, H.J. Snaith, D. Cahen, Photovoltaic solar cell technologies: analysing the state of the art, Nat. Rev. Mater. 4 (4) (2019) 269–285.
[8] N.S. Lewis, Introduction: solar energy conversion, Chem. Rev. 115 (23) (2015) 12631–12632.
[9] M. Zhu, S. Kim, L. Mao, M. Fujitsuka, J. Zhang, X. Wang, T. Majima, Metal-free photocatalyst for H_2 evolution in visible to near-infrared region: black phosphorus/graphitic carbon nitride, J. Am. Chem. Soc. 139 (37) (2017) 13234–13242.
[10] S. Zhu, D. Wang, Photocatalysis: basic principles, diverse forms of implementations and emerging scientific opportunities, Adv. Energy Mater. 7 (23) (2017), 1700841.
[11] S. Weon, F. He, W. Choi, Status and challenges in photocatalytic nanotechnology for cleaning air polluted with volatile organic compounds: visible light utilization and catalyst deactivation, Environ. Sci. Nano 6 (11) (2019) 3185–3214.
[12] R. Asahi, T. Morikawa, H. Irie, T. Ohwaki, Nitrogen-doped titanium dioxide as visible-light-sensitive photocatalyst: designs, developments, and prospects, Chem. Rev. 114 (19) (2014) 9824–9852.
[13] M.-Q. Yang, M. Gao, M. Hong, G.W. Ho, Visible-to-NIR photon harvesting: progressive engineering of catalysts for solar-powered environmental purification and fuel production, Adv. Mater. 30 (47) (2018), 1802894.
[14] A.V. Akimov, A.J. Neukirch, O.V. Prezhdo, Theoretical insights into photoinduced charge transfer and catalysis at oxide interfaces, Chem. Rev. 113 (6) (2013) 4496–4565.
[15] S. Hu, M.R. Shaner, J.A. Beardslee, M. Lichterman, B.S. Brunschwig, N.S. Lewis, Amorphous TiO_2 coatings stabilize Si, GaAs, and GaP photoanodes for efficient water oxidation, Science 344 (6187) (2014) 1005–1009.
[16] K. Lee, A. Mazare, P. Schmuki, One-dimensional titanium dioxide nanomaterials: nanotubes, Chem. Rev. 114 (19) (2014) 9385–9454.
[17] A. Naldoni, M. Altomare, G. Zoppellaro, N. Liu, Š. Kment, R. Zbořil, P. Schmuki, Photocatalysis with Reduced TiO_2: From Black TiO_2 to Cocatalyst-Free Hydrogen Production, ACS Catal. 9 (1) (2019) 345–364.
[18] Z. Lin, J. Wang, Introduction, in: Z. Lin, J. Wang (Eds.), Low-cost Nanomaterials: Toward Greener and More Efficient Energy Applications, Springer London, London, 2014, pp. 1–7.
[19] X. Ren, P. Gao, X. Kong, R. Jiang, P. Yang, Y. Chen, Q. Chi, B. Li, NiO/Ni/TiO_2 nanocables with Schottky/p-n heterojunctions and the improved photocatalytic performance in water splitting under visible light, J. Colloid Interface Sci. 530 (2018) 1–8.
[20] S.A. Al-Thabaiti, R. Hahn, N. Liu, R. Kirchgeorg, S. So, P. Schmuki, S.N. Basahel, S. M. Bawaked, NH_3 treatment of TiO_2 nanotubes: from N-doping to semimetallic conductivity, Chem. Commun. 50 (59) (2014) 7960–7963.
[21] X. Kang, S. Liu, Z. Dai, Y. He, X. Song, Z. Tan, Titanium dioxide: from engineering to applications, Catalysts 9 (2) (2019) 191.
[22] M.I. Litter, E. San Román, M.A. Grela, J.M. Meichtry, H.B. Rodríguez, Sensitization of TiO_2 by dyes: a way to extend the range of photocatalytic activity of TiO_2 to the visible region, Visible Light-Act. Photocatal. (2018) 253–282.
[23] Y. Bai, Y. Zhou, J. Zhang, X. Chen, Y. Zhang, J. Liu, J. Wang, F. Wang, C. Chen, C. Li, R. Li, C. Li, Homophase junction for promoting spatial charge separation in photocatalytic water splitting, ACS Catal. 9 (4) (2019) 3242–3252.
[24] K.M. Mayer, J.H. Hafner, Localized surface plasmon resonance sensors, Chem. Rev. 111 (6) (2011) 3828–3857.
[25] A.B. Tesler, L. Chuntonov, T. Karakouz, T.A. Bendikov, G. Haran, A. Vaskevich, I. Rubinstein, Tunable localized plasmon transducers prepared by thermal dewetting of percolated evaporated gold films, J. Phys. Chem. C 115 (50) (2011) 24642–24652.
[26] M. Svedendahl, S. Chen, M. Käll, An introduction to plasmonic refractive index sensing, in: A. Dmitriev (Ed.), Nanoplasmonic Sensors, Springer New York, New York, NY, 2012, pp. 1–26.
[27] N.T. Nguyen, M. Altomare, J.E. Yoo, N. Taccardi, P. Schmuki, Noble metals on anodic TiO_2 nanotube mouths: thermal dewetting of minimal Pt Co-catalyst loading leads to significantly enhanced photocatalytic H_2 generation, Adv. Energy Mater. 6 (2) (2016), 1501926.
[28] D. Tsukamoto, Y. Shiraishi, Y. Sugano, S. Ichikawa, S. Tanaka, T. Hirai, Gold nanoparticles located at the interface of anatase/rutile TiO_2 particles as active plasmonic photocatalysts for aerobic oxidation, J. Am. Chem. Soc. 134 (14) (2012) 6309–6315.
[29] L. Qin, G. Zeng, C. Lai, D. Huang, C. Zhang, M. Cheng, H. Yi, X. Liu, C. Zhou, W. Xiong, F. Huang, W. Cao, Synthetic strategies and application of gold-based nanocatalysts for nitroaromatics reduction, Sci. Total Environ. 652 (2019) 93–116.
[30] A.B. Tesler, B.M. Maoz, Y. Feldman, A. Vaskevich, I. Rubinstein, Solid-state thermal dewetting of just-percolated gold films evaporated on glass: development of the morphology and optical properties, J. Phys. Chem. C 117 (21) (2013) 11337–11346.
[31] A.B. Tesler, T. Sannomiya, A. Vaskevich, E. Sabatani, I. Rubinstein, Highly sensitive colorimetric detection of early stage aluminum corrosion in water using plasmonic gold nanoparticle films, Adv. Opt. Mater. 6 (21) (2018), 1800599.
[32] M. Altomare, N.T. Nguyen, P. Schmuki, Templated dewetting: designing entirely self-organized platforms for photocatalysis, Chem. Sci. 7 (12) (2016) 6865–6886.

[33] S. Mubeen, S. Zhang, N. Kim, S. Lee, S. Krämer, H. Xu, M. Moskovits, Plasmonic properties of gold nanoparticles separated from a gold mirror by an ultrathin oxide, Nano Lett. 12 (4) (2012) 2088–2094.

[34] Y. Fang, Y. Jiao, K. Xiong, R. Ogier, Z.-J. Yang, S. Gao, A.B. Dahlin, M. Käll, Plasmon enhanced internal photoemission in antenna-spacer-mirror based Au/TiO_2 nanostructures, Nano Lett. 15 (6) (2015) 4059–4065.

[35] F. Benz, R. Chikkaraddy, A. Salmon, H. Ohadi, B. de Nijs, J. Mertens, C. Carnegie, R.W. Bowman, J.J. Baumberg, SERS of individual nanoparticles on a mirror: size does matter, but so does shape, J. Chem. Phys. Lett. 7 (12) (2016) 2264–2269.

[36] L. Li, T. Hutter, U. Steiner, S. Mahajan, Single molecule SERS and detection of biomolecules with a single gold nanoparticle on a mirror junction, Analyst 138 (16) (2013) 4574–4578.

[37] C.-H. Lai, G.-A. Wang, T.-K. Ling, T.-J. Wang, P.-k Chiu, Y.-F. Chou Chau, C.-C. Huang, H.-P. Chiang, Near infrared surface-enhanced Raman scattering based on star-shaped gold/silver nanoparticles and hyperbolic metamaterial, Sci. Rep. 7 (1) (2017) 5446.

[38] G. Zhao, H. Kozuka, T. Yoko, Sol-gel preparation and photoelectrochemical properties of TiO_2 films containing Au and Ag metal particles, Thin Solid Films 277 (1) (1996) 147–154.

[39] C. Ng, J.J. Cadusch, S. Dligatch, A. Roberts, T.J. Davis, P. Mulvaney, D.E. Gómez, Hot carrier extraction with plasmonic broadband absorbers, ACS Nano 10 (4) (2016) 4704–4711.

[40] X. Shi, K. Ueno, T. Oshikiri, H. Misawa, Improvement of plasmon-enhanced photocurrent generation by interference of TiO_2 thin film, J. Phys. Chem. C. 117 (47) (2013) 24733–24739.

[41] X. Shi, K. Ueno, T. Oshikiri, Q. Sun, K. Sasaki, H. Misawa, Enhanced water splitting under modal strong coupling conditions, Nat. Nanotechnol. 13 (10) (2018) 953–958.

[42] S. Eustis, M.A. El-Sayed, Why gold nanoparticles are more precious than pretty gold: noble metal surface plasmon resonance and its enhancement of the radiative and nonradiative properties of nanocrystals of different shapes, Chem. Soc. Rev. 35 (3) (2006) 209–217.

[43] V.G. Kravets, A.V. Kabashin, W.L. Barnes, A.N. Grigorenko, Plasmonic surface lattice resonances: a review of properties and applications, Chem. Rev. 118 (12) (2018) 5912–5951.

[44] C. Lee, Y. Park, J.Y. Park, Hot electrons generated by intraband and interband transition detected using a plasmonic Cu/TiO_2 nanodiode, RSC Adv. 9 (32) (2019) 18371–18376.

[45] A.W. Dweydari, C.H.B. Mee, Work function measurements on (100) and (110) surfaces of silver, Phys. Status Solidi A 27 (1) (1975) 223–230.

[46] X.D. Gao, G.T. Fei, S.H. Xu, B.N. Zhong, H.M. Ouyang, X.H. Li, L.D. Zhang, Porous Ag/TiO_2-Schottky-diode based plasmonic hot-electron photodetector with high detectivity and fast response, Nanophotonics 8 (7) (2019) 1247–1254.

[47] M. Bernardi, J. Mustafa, J.B. Neaton, S.G. Louie, Theory and computation of hot carriers generated by surface plasmon polaritons in noble metals, Nat. Commun. 6 (1) (2015) 7044.

[48] C.V. Thompson, Solid-state dewetting of thin films, Annu. Rev. Mater. Res. 42 (1) (2012) 399–434.

[49] I. Doron-Mor, Z. Barkay, N. Filip-Granit, A. Vaskevich, I. Rubinstein, Ultrathin gold island films on silanized glass. morphology and optical properties, Chem. Mater. 16 (18) (2004) 3476–3483.

[50] M. Lickleder, R. Mohammadi, N.T. Nguyen, H. Park, S. Hejazi, M. Halik, N. Vogel, M. Altomare, P. Schmuki, Dewetted Au nanoparticles on TiO_2 surfaces: evidence of a size-independent plasmonic photoelectrochemical response, J. Phys. Chem. C 123 (27) (2019) 16934–16942.

[51] X. Zhou, E. Wierzbicka, N. Liu, P. Schmuki, Black and white anatase, rutile and mixed forms: band-edges and photocatalytic activity, Chem. Commun. 55 (4) (2019) 533–536.

[52] A.E.R. Mohamed, S. Barghi, S. Rohani, N- and C-modified TiO_2 nanotube arrays: enhanced photoelectrochemical properties and effect of nanotubes length on photoconversion efficiency, Nanomaterials 8 (4) (2018) 198.

[53] M. Svedendahl, M. Käll, Fano interference between localized plasmons and interface reflections, ACS Nano 6 (8) (2012) 7533–7539.

[54] S. Ozkan, N.T. Nguyen, A. Mazare, P. Schmuki, Optimized spacing between TiO_2 nanotubes for enhanced light harvesting and charge transfer, ChemElectroChem 5 (21) (2018) 3183–3190.

[55] T. Karakouz, A.B. Tesler, T.A. Bendikov, A. Vaskevich, I. Rubinstein, Highly stable localized plasmon transducers obtained by thermal embedding of gold island films on glass, Adv. Mater. 20 (20) (2008) 3893–3899.

[56] D.C. Ratchford, Plasmon-induced charge transfer: challenges and outlook, ACS Nano 13 (12) (2019) 13610–13614.

[57] G. Tagliabue, A.S. Jermyn, R. Sundararaman, A.J. Welch, J.S. DuChene, R. Pala, A. R. Davoyan, P. Narang, H.A. Atwater, Quantifying the role of surface plasmon excitation and hot carrier transport in plasmonic devices, Nat. Commun. 9 (1) (2018) 3394.

[58] L.V. Besteiro, X.-T. Kong, Z. Wang, G. Hartland, A.O. Govorov, Understanding hot-electron generation and plasmon relaxation in metal nanocrystals: quantum and classical mechanisms, ACS Photonics 4 (11) (2017) 2759–2781.

[59] G.V. Hartland, L.V. Besteiro, P. Johns, A.O. Govorov, What's so hot about electrons in metal nanoparticles? ACS Energy Lett. 2 (7) (2017) 1641–1653.

[60] S. Linic, P. Christopher, D.B. Ingram, Plasmonic-metal nanostructures for efficient conversion of solar to chemical energy, Nat. Mater. 10 (12) (2011) 911–921.

[61] D. Pillay, Y. Wang, G.S. Hwang, A comparative theoretical study of Au, Ag and Cu adsorption on TiO_2 (110) rutile surfaces, Korean J. Chem. Eng. 21 (2) (2004) 537–547.

[62] D. Spanu, S. Recchia, S. Mohajernia, O. Tomanec, Š. Kment, R. Zboril, P. Schmuki, M. Altomare, Templated dewetting–alloying of NiCu bilayers on TiO_2 nanotubes enables efficient noble-metal-free photocatalytic H_2 evolution, ACS Catal. 8 (6) (2018) 5298–5305.

[63] M.D. Susman, A. Vaskevich, I. Rubinstein, A general kinetic-optical model for solid-state reactions involving the nano kirkendall effect. the case of copper nanoparticle oxidation, J. Phys. Chem. C 120 (29) (2016) 16140–16152.

[64] R.P. Lynch, A. Ghicov, P. Schmuki, A. Photo-Electrochemical, Investigation of self-organized TiO_2 nanotubes, J. Electrochem. Soc. 157 (3) (2010) G76.

[65] H. Zhu, H. Xie, Y. Yang, K. Wang, F. Zhao, W. Ye, W. Ni, Mapping hot electron response of individual gold nanocrystals on a TiO_2 photoanode, Nano Lett. 20 (4) (2020) 2423–2431.

[66] S.-S. Liu, L.C. Saha, A. Iskandarov, T. Ishimoto, T. Yamamoto, Y. Umeno, S. Matsumura, M. Koyama, Atomic structure observations and reaction dynamics simulations on triple phase boundaries in solid-oxide fuel cells, Commun. Chem. 2 (1) (2019) 48.

[67] E. Cottancin, G. Celep, J. Lermé, M. Pellarin, J.R. Huntzinger, J.L. Vialle, M. Broyer, Optical properties of noble metal clusters as a function of the size: comparison between experiments and a semi-quantal theory, Theor. Chem. Acc. 116 (4) (2006) 514–523.

[68] Z. Chen, T.G. Deutsch, H.N. Dinh, K. Domen, K. Emery, A.J. Forman, N. Gaillard, R. Garland, C. Heske, T.F. Jaramillo, A. Kleiman-Shwarsctein, E. Miller, K. Takanabe, J. Turner, Introduction, photoelectrochemical water splitting: standards. Experimental Methods, and Protocols, Springer New York,, New York, NY, 2013, pp. 1–5.

[69] B.Y. Zheng, H. Zhao, A. Manjavacas, M. McClain, P. Nordlander, N.J. Halas, Distinguishing between plasmon-induced and photoexcited carriers in a device geometry, Nat. Commun. 6 (1) (2015) 7797.

[70] A.J. Leenheer, P. Narang, N.S. Lewis, H.A. Atwater, Solar energy conversion via hot electron internal photoemission in metallic nanostructures: Efficiency estimates, J. Appl. Phys. 115 (13) (2014), 134301.

[71] P.B. Johnson, R.W. Christy, Optical constants of transition metals: Ti, V, Cr, Mn, Fe, Co, Ni, and Pd, Phys. Rev. B 9 (12) (1974) 5056–5070.

[72] T. Siefke, S. Kroker, K. Pfeiffer, O. Puffky, K. Dietrich, D. Franta, I. Ohlídal, A. Szeghalmi, E.-B. Kley, A. Tünnermann, Materials pushing the application limits of wire grid polarizers further into the deep ultraviolet spectral range, Adv. Opt. Mater. 4 (11) (2016) 1780–1786.